Contrib Mineral Petrol (2012) 164:959–976
DOI 10.1007/s00410-012-0782-0

ORIGINAL PAPER

Settling and compaction of olivine in basaltic magmas: an experimental study on the time scales of cumulate formation

Max W. Schmidt · Melanie Forien · Giulio Solferino · Nickolai Bagdassarov

Received: 6 October 2010 / Accepted: 6 July 2012 / Published online: 2 August 2012

Abstract A series of centrifuge-assisted settling experiments of 30 vol % olivine in 70 vol % basaltic melt was conducted to elucidate the formation mechanisms and time scales of gravitational cumulates. The settling experiments were performed in a centrifuging piston cylinder at 200–1,500*g*, 1,270–1,280 °C, and 0.8–1.1 GPa on previously annealed and texturally equilibrated samples. The mechanical settling of the dense olivine suspension occurs at about 1/6 the speed of simple Stokes settling, resulting in a sedimentation exponent $n = 4.1(6)$ in agreement with predictions from analogue systems. The porosity (φ_m) of the orthocumulate resulting from gravitational settling of crystals is about 54 % and formation times of olivine orthocumulates result to 0.1–10 m day^{-1} (for an initial crystal content of the melt of 1–5 % and grain sizes of 2–10 mm). After mechanical settling, olivine grains rest on each other, and further compaction occurs through pressure dissolution at grain contacts, olivine reprecipitation where olivine is in contact with melt, and concomitant expulsion of excess liquid from the cumulate layer. With centrifugation at 400*g* for 50 h, porosities as low as 30.3 vol % were achieved. The olivine content at the bottom of the gravitational cumulate is $1 - \varphi_m \sim \log(\Delta\rho \cdot h \cdot a \cdot t)$, where $\Delta\rho$ is the density difference between crystals and melt, h the crystal layer thickness, a the acceleration, and t the time of centrifuging. Compaction is hence proportional to effective stress integrated over time indicating that pressure dissolution is the dominant mechanism for chemical compaction. The compaction limit, that is the lowermost porosity to be reached by this mechanism, is calculated by equating the lithostatic and hydraulic pressure gradients in the cumulate and results to 3–5 % porosity for the experiments. Crystal size distribution curves and a growth exponent n of 3.1(3) indicate that diffusion-controlled Ostwald ripening is the dominant crystal growth mechanism. The above relationship, combined with a linear scaling for grain size as appropriate for reaction-controlled pressure solution creep, allows calculation of formation times of adcumulates. If chemical compaction is dissolution–reprecipitation limited, then single layers of natural olivine adcumulates of ½ m thickness with 70–75 vol % olivine at the base (as observed in the Rhum layered intrusion) would have typical formation times of 0.4–3 years for grain sizes of 2–10 mm. This time scale compares favourably with characteristic cooling times of sills. If a greater than 20-m-thick series of cumulate layers pressurizes a base layer with the porosity still filled by a melt, then compaction proceeds to the compaction limit within a few years. It can thus be expected that in layered mafic intrusions where cumulates are continuously deposited from a large magma chamber and which characteristic cooling times of more than

Communicated by J. Hoefs.

M. W. Schmidt (✉) · G. Solferino
Institute of Geochemistry and Petrology, ETH, Clausiusstrasse 25, 8092 Zurich, Switzerland
e-mail: max.schmidt@erdw.ethz.ch

M. Forien · N. Bagdassarov
Institut für Geowissenschaften/Facheinheit Geophysik, J.W. Goethe Universität, Altenhöferallee 1, 60438 Frankfurt am Main, Germany

Present Address:
M. Forien
Institut des Sciences de la Terre, CNRS, Orléans, France

Present Address:
G. Solferino
Department of Earth Science, St. Francis Xavier University, Antigonish, NS, Canada

decades, a compaction zone of several tens of metres forms with adcumulates only maintaining porosities in the order of 5 %. In conclusion, gravitational settling and gravitation-driven chemical compaction are feasible cumulate-forming processes for dense mafic minerals in basaltic magmas and in particular in large layered intrusions.

Keywords Grain settling · Gravitational cumulate · Chemical compaction · Centrifuge

Introduction

Gravitational cumulates form in crystallizing magma chambers, sills, or lava lakes of typically mafic to ultramafic composition. In such layered intrusions, gravitational accumulation of generally downward settling silicates, oxides, or sulphides has been proposed as the dominant mechanism forming cumulate layers sometimes extending over >100 km and involving magma volumes of several km^3. The most famous layered intrusions include Skaergaard (Greenland), Bushveld (South Africa), Stillwater (Montana), Muskox (Canada), and Windimura (Australia) (Wager and Brown 1968), most of them being of large economical interest due to the high concentration of metals (e.g. Cr, V, Au, Pt, Pd) in specific layers. Whether gravitational settling of crystals followed by pressure-driven chemical compaction is the dominant mechanism in the formation of such layering is matter of debate (Raedecke and McCallum 1984; Irvine 1987; Boudreau and McBirney 1997; Irvine et al. 1998). Other cumulate-forming mechanisms include density currents (Wager and Brown 1968; Irvine 1987; Conrad and Naslund 1989), magma chamber recharge and mixing (Gasquet et al. 1995; Lucas and St-Onge 1995), temperature oscillations across a cotectic (Lesher and Walker 1988), in situ crystallization from a boundary (McBirney and Noyes 1979; Langmuir 1989), layers with double-diffusive convection (McBirney and Noyes 1979; Chen and Turner 1980; Kerr and Turner 1982; Irvine et al. 1983; Huppert and Sparks 1984; Wilson and Larsen 1985; Wilson et al. 1987; Robins et al. 1987), and preferential or oscillatory nucleation (Wager 1959; Hort et al. 1993), or any combination of the above. Illustrated examples of such magma chamber processes can be found in the study by Parsons (1987), McBirney and Nicolas (1997), Boudreau and McBirney (1997), and a discussion on cumulate-forming mechanisms in the study by Naslund and McBirney (1996).

The formation of cumulates has been mostly investigated from field data (Wager et al. 1960; Holness et al. 2005), analogue experiments (Schwindinger 1999), and numerical modelling (Akatsuka et al. 1999; Hoshide et al. 2006; Tory and Pickard 1977, 1986). Mineralogically, cumulate layering is termed cryptic when defined through changes in composition of the constituting mineral(s). In contrast, phase layering describes the abrupt entrance or exit of cumulus minerals at particular horizons of the sequence. Texturally, cumulates are defined as orthocumulates when grains are just barely in contact and the residual melt fraction crystallized between the accumulated grains. In contrast, adcumulates are characterized by very small melt fractions crystallized between the accumulated grains (Wager et al. 1960). Orthocumulates are thought to be formed by purely mechanical accumulation of grains, the maximum solid fraction of the gravitationally settling mineral(s) theoretically corresponding to the maximum close packing for a solid with the shape of the crystallizing phase(s). Nevertheless, in practice, observed porosities of orthocumulates are in the order of 60 % (Tegner et al. 2009). Mechanisms leading to orthocumulates include not only Stokes settling of crystals in a magmatic suspension but also gravity slumps and density currents.

Contrasting orthocumulates, meso- and adcumulates (Wager et al. 1960) form by densification of orthocumulates. Adcumulus growth is a process mainly driven by chemical compaction during which grains grow at the expense of liquid trapped between early crystals without crystallizing from that liquid, that is, crystals change their shape thus reducing pore space and liquid is expelled from the crystal layer. The latter may then result in an increase in the crystal fraction to up to 80 %, in Rhum, where the olivine content of cumulates reaches ~80 vol % (Wager and Brown 1968) or to ~95 % as in Skaegaard, where the residual porosity in the Upper and Middle Zones are reduced to 3–7 % (Tegner et al. 2009). Both types of cumulates can be found together or separated in the Rhum intrusion, the Bushveld complex, and the Skaergaard complex.

Centrifugation as a means to study crystal settling and cumulate formation in magmas at atmospheric pressure was pioneered by Roeder and Dixon (1977) and Kadik et al. (1989), both rotating a 1-atm furnace without and with controlled atmosphere, respectively. Centrifugation at pressure was introduced by Dorfman et al. (1997), which mounted an externally heated autoclave capable of 100 MPa into a biological centrifuge. More recently, a piston cylinder was mounted onto a centrifuge by Schmidt et al. (2006) extending the range of centrifuging pressures to 1.7 GPa.

In this study, we experimentally form cumulate layers of olivine from suspensions in basaltic melt first by mechanical and then by chemical compaction. This permits evaluation of the mechanisms and formation times of ortho- and adcumulates for which gravitation is the driving force. While the concepts of settling and compaction are intriguingly simple, they pose hideous experimental problems. At 1 g, buoyancy forces on crystals in silicate melts

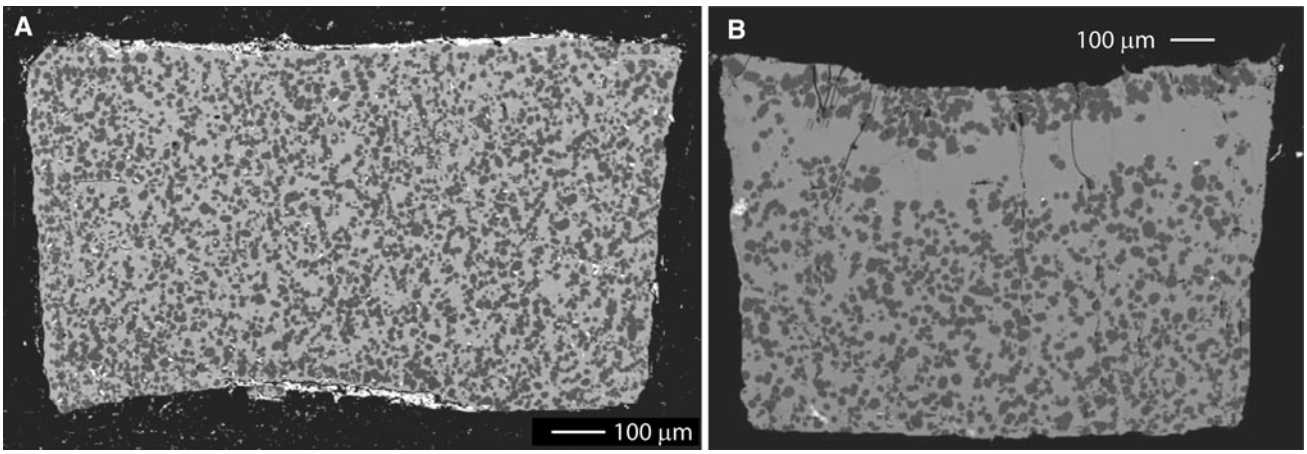

Fig. 1 BSE images of static experiments. **a** OB-14 (1 g, 24 h), **b** OB-6 (1 g, 72 h). The dark grey phase is olivine, and the light *grey* phase basaltic melt. The *black* surrounding is the graphite capsule, and white speckles correspond to electrostatic charging. The starting material is a homogeneous mixture of 70 vol % MORB glass and 30 vol % olivine with a grain size of 1.8 µm. Both experiments resulted in 65 vol % melt, and the texture of the 24-h experiment (**a**) corresponds to the starting point of the centrifuge experiments. Note the uneven, most likely temperature gradient-dependent distribution of crystals in the longer run (**b**)

do not dominate crystal distributions in experimental systems. Instead, the experimentally unavoidable temperature gradients of even 1–2 degrees centigrade/mm cause chemical diffusion due to saturation gradients; crystals dissolve in the hot zone of a capsule and reprecipitate in the cold zone, resulting in a mostly temperature dominated rearrangement of crystals at ambient gravity (Lesher and Walker 1988, see Fig. 1). Further complexity arises from Soret diffusion, also induced by temperature gradients (Chipman 1926; Lesher and Walker 1988; Cygan and Carrigan 1992). To overcome the effects of temperature gradients on crystal distribution, gravitational forces have been amplified by employing the centrifuging piston cylinder at 400–1,500*g*.

The goal of this study is not to decide which cumulate formation mechanism is prevalent in nature, rather it is to investigate the mechanics and time scale of gravitationally driven crystal settling and compaction to understand the feasibility of this process for (layered) intrusions.

Experimental and analytical techniques

Experimental strategy

First, static equilibration experiments were performed on a mixture of 30 vol % olivine and 70 vol % melt to obtain equilibrated textures and crystal shapes and to measure crystal size and crystal distribution at the starting point of the centrifuge settling experiment. After establishing a satisfying experimental protocol to obtain a homogeneous initial crystal distribution, each further experimental charge was first statically equilibrated following this protocol. The capsules from the static equilibration experiments were then reloaded into the centrifuging piston cylinder, heated to the same temperature, and then centrifuged for the desired amount of time and gravity acceleration.

Experimental techniques

The starting material was a 30:70 vol % olivine/MORB mixture of natural San Carlos olivine and synthetic simplified MORB glass with a Mg# of 79 (Table 1). Olivine powder was obtained through crushing and subsequent milling for a few hours. Additionally, after initial milling, grains larger than 10 µm were removed by sieving, a procedure that allowed to obtain a narrow grain size spectrum for the starting olivine. The final grain size was measured through laser diffractometry on dispersed solutions ("Mastersizer 2000" instrument, Malvern Instruments Ltd.).

Table 1 Melt and crystal starting compositions, in wt%

Oxides	MORB	San Carlos	Melt-OB6	Olivine-OB6
SiO_2	51.8	41.0	50.2	40.1
TiO_2	2.52	0	2.30	0.07
Al_2O_3	14.9	0	13.7	0.08
FeO	5.19	8.96	6.20	7.18
MnO	0.04	0.23	0.07	0.06
MgO	11.4	49.8	13.9	52.1
CaO	11.3	0	11.2	0.30
Na_2O	1.92	0	1.95	0.02
K_2O	0.53	0	0.50	0
Total	99.6	100.0	100.0	100.0
Mg#	79.7	90.8	80.0	92.2

Table 2 Run conditions

Experiment	T (°C)	P (GPa)	Static run time (h)	Acceleration (a) (× 9,81 m/s)	Centrifuging time (t) (h)	$a * t$ (m/s)	Height crystal layer (h)[a] (μm)	Total porosity crystal layer (vol %)	Porosity bottom layer (vol %)	Initial grain size (μm)	Final mean grain size (μm)
OB-14	1,270	1.0	24	1	–	–	–	65.9 (2.1)	67.1 (2.1)	1.8	13.1 (2.5)
OB-6	1,270	1.0	72	1	–	–	–	64.5 (2.0)	64.0 (2.1)	1.8	19.1 (2.4)
ZOB 9	1,280	1.0	21	200	1.00	0.72×10^6	620	53.5 (4.1)	51.6 (1.7)	1.8	13.1 (5.3)
ZOB 6	1,280	0.8	20	200	3.00	2.16×10^6	625	55.3 (2.4)	51.2 (2.1)	1.8	13.3 (2.5)
ZOB 1	1,280	1.1	22	400	6.00	8.64×10^6	450	49.9 (2.4)	45.5 (1.8)	1.8	14.4 (2.5)
ZOB 11	1,280	1.0	21	1,500	1.67	9.00×10^6	640	38.2 (3.0)	35.4 (2.3)	1.8	11.0 (6.6)
ZOB 5	1,280	0.9	21	700	10.00	25.2×10^6	450	42.5 (2.0)	37.1 (1.9)	1.8	14.7 (2.1)
ZOB 10	1,280	1.0	275	1,500	4.67	25.2×10^6	420	38.9 (4.3)	37.3 (2.4)	1.8	12.3 (5.3)[b]
ZOB 4	1,280	0.9	21	400	50.00	72.0×10^6	560	36.7 (2.1)	30.3 (2.0)	1.8	18.6 (2.3)
FF01	1,280	1.0	72	700	10.00	25.2×10^6	740	42.1 (2.0)	42.5 (4.4)	26	33
FF05	1,280	1.0	72	700	10.00	25.2×10^6	730	43.4 (1.0)	37.4 (5.4)	36	47
FF04	1,280	1.0	72	700	10.00	25.2×10^6	730	43.5 (1.4)	41.9 (5.6)	51.5	64

[a] Height of crystal layer above the centre of the bottom segment within the crystal pile

[b] This experiment contains one large 500 μm grain, which is not considered for the mean grain size

The grain size distribution curve of the starting olivine for the OB and ZOB series (Table 2) yields an average size of ~1.8 μm with a 1σ deviation of ±0.5 μm. For a second series (FF, Table 2), initial grain sizes were varied and were 26, 36, and 51.5 μm. The MORB glass was obtained from melting synthetic oxide powders at 1,300 °C and an oxygen fugacity of log (f_{O_2}) = −6.704 yielding an Fe^{3+}/Fe^{2+} ratio corresponding to QFM at 1,300 °C, 1 GPa. The glass was then crushed, milled, and thoroughly mixed with olivine.

Static equilibration experiments were performed in an end-loaded piston cylinder with a 14-mm bore, employing double Pt-graphite capsules with an outer diameter of 4 mm and an inner diameter and height of 2.0 and 1.0 mm. Piston cylinder assemblies consisted of external NaCl and Pyrex sleeves, a straight graphite furnace (6.0 mm I.D., 36 mm length), and inner crushable MgO cylinders containing the capsule and mullite thermocouple ceramics. B-type Pt–Rh thermocouples were separated from the Pt-capsule by a 0.6-mm corundum disc and temperature controlled with an accuracy of ±5 °C. Pressure was calibrated against fayalite + quartz = orthoferrosilite (Bohlen et al. 1980) and the quartz–coesite transition (Bose and Ganguly 1995). Temperature was ramped down manually with a rate of ca. 50 °C/s. Static equilibration experiments were carried out at 1,270 or 1,280 °C and 1.0 GPa (Table 2). For the textural equilibration, these conditions were kept for 20–24 h for an initial grain size of 1.8 μm, 72 h for larger grain sizes (FF series, Table 2), and in one case 275 h (Table 2). The latter experiment was intended to grow large grains, but resulted in one ~500 μm grain stuck to the capsule roof and a rather homogeneous reminder of nicely settled crystals of 12.3 ± 5.3 μm (after centrifugation).

The centrifuging piston cylinder is a 42-kg single-stage piston cylinder with the same bore diameter and assembly as for the static runs (Schmidt et al. 2006). This piston cylinder is mounted into a rotating table such that the assembly axis is radial, the thermocouple towards the centre, the bottom of the metal capsule facing the thermocouple, acceleration thus being directed towards the metal capsule lid. The inner graphite capsule has its lid towards the thermocouple (also during the static experiments), such that acceleration is directed towards the bottom of the graphite capsule. In the centrifuge, the sample is located at a radius of 32 cm, the maximum acceleration used in this study of 1,500g being reached at 2,030 revolutions per minute (rpm). Centrifuge experiments were carried out at 1,270–1,280 °C, 0.8–1.1 GPa, and accelerations of 200–1,500g for a maximum duration of 50 h. Heating through the slip ring stack of the centrifuge is only advisable when the table is rotating and thus centrifuge experiments include two steps: first, the piston cylinder is pressurized to 0.4 GPa, the table run at 200 rpm (15 g), and the assemblage heated to soften the Pyrex glass and collapse the assembly's porosity at 600 °C. Temperature is then ramped down, the table stopped, and pressure increased such that after heating and thermal equilibration of the assembly, the desired final 1.0 GPa is achieved. The somewhat variable final run pressure (Table 2) results from the fact that this procedure was established during this series of experiments and that pressure adjustment during centrifugation is not possible, thus necessarily allowing for

the characteristic pressure losses of salt + Pyrex assemblies with time. Nevertheless, the amount of crystals in the olivine + MORB system is fairly insensitive to small pressure fluctuations, the latter thus do not influence our experimental results (see also Connolly et al. 2009).

Analytical techniques

Polished sections of the run products were imaged with backscattered electrons (BSE) and chemically characterized with wavelength dispersive spectrometry (WDS) employing a Jeol JXA-8200 electron microprobe. WDS analyses of olivine were operated with a 15 kV, 20 nA focused beam. For melt analyses, 15 kV, 5 nA, and a beam size of 10 μm were employed.

Melt abundances along the capsule were obtained through digital analysis of BSE images with the software "Image Tool" (UTHSCSA Image Tool, The University of Texas Health Science Center in San Antonio). For this purpose, BSE images were converted to binary images. The crystal bearing part of the capsule was then sliced in 4–7 segments of approximately 100 μm height perpendicular to the capsule axis (the crystal layer amounting to 420–740 μm) and the area of each segment was analysed for crystal size and content. We tested different segment heights (between 60 and 150 μm) and found that segments of ~100 μm height gave statistically well-defined results in that lateral sectioning of a segment into two or several sub-areas yielded results identical within error. Image analysis was repeated three times for several areas on each sample to evaluate average errors on melt abundances within a segment. Measurements of melt abundances in the crystal layer were limited to the axial region (50–60 % of the capsule diameter) to avoid boundary effects when settling crystals or raising liquid interfere with the capsule walls (Botto et al. 2005; Tatum et al. 2005). Further through the manuscript we refer to the top segment, second segment and bottom segment as counted from the gravitational top of the crystal pile. To calculate the effective pressure in the centre of the bottom segment, half a segment height is subtracted from the total height of all segments (given in Table 2).

Results

Crystal distribution after static equilibration

The static equilibration experiments did result in a homogeneous spatial distribution of crystals if limited to 24 h at 1,270–1,280 °C (Fig. 1a). After 24 h, the average grain size grows from 1.8 ± 0.5 μm to 13.1 ± 2.5 μm. The melt content is then 65.9 ± 2.1 vol %, which compares to 70 vol % melt in the starting material. The small difference in melt percentage is readily explained with a temperature-dependent solubility of olivine, our starting basalt melt being slightly oversaturated in olivine at 1,270 °C. The crystal size and spatial distribution as shown in Fig. 1a represent the texture of our sample when starting centrifuging.

Longer static equilibration times of 72 h led to an increased average grain size of 19.1 ± 2.4 μm and result unavoidably in an uneven distribution of olivine within the capsule (Fig. 1b). Olivine grains formed a dispersed and homogeneous layer in the lower 2/3 of the capsule, but a zone with significantly less crystals in the upper part and a zone with crystals above average grain size at the capsule top. The Stokes settling velocity for olivines of 13–19 μm diameter in a basaltic liquid at 1,280 °C is 8.2 to 17.5 μm/h, which could, after 72 h, account for a pure melt zone of about 150 μm height for grains growing with time to their final size. However, a dense suspension of crystals with a crystal fraction of ~0.3 settles only at about 1/10 of the Stokes velocity (Schwindinger 1999, see also Sect. "Stokes settling velocity"), and secondly, the crystal poor zone forms within the suspension and not at the top. We thus conclude that the crystal poor zone forms through a chemical rather than mechanical process. Most likely, this zone corresponds to the hot zone in the capsule where crystals are dissolved due to saturation gradients and then reprecipitated during grain growth in the adjacent colder regions (Lesher and Walker 1988). Clearly, long static experiments lead to a spatial crystal distribution that is not governed by simple gravitational crystal settling.

Porosity profiles through the olivine layer after centrifuging

Statically annealed, homogeneous, and texturally equilibrated samples (as in Fig. 1a) were centrifuged with varying acceleration and centrifugation time from 200 to 1,500*g* and from 1 to 50 h (Table 2). Except the settling experiment ZOB9, all other centrifuge experiments caused the total of the crystals to accumulate in a single olivine layer, leaving a homogeneous crystal-free basalt melt layer in the gravitational top of the capsule (Fig. 2). This top melt layer is of no further interest to this study. Porosity profiles through the cumulate layer are given in Fig. 3. The porosity obtained after Stokes settling of the olivine crystals was ~54 % (ZOB6, ZOB9), and the most compacted basal crystal layer had a porosity of 30 % (ZOB 4). For the experiments starting from 1.8 μm grain size, these profiles show a linear porosity (φ) versus height (h) relation when excluding the uppermost segment which has a significantly higher porosity (Fig. 3a). Absolute porosities determined from image analysis have analytical errors of typically

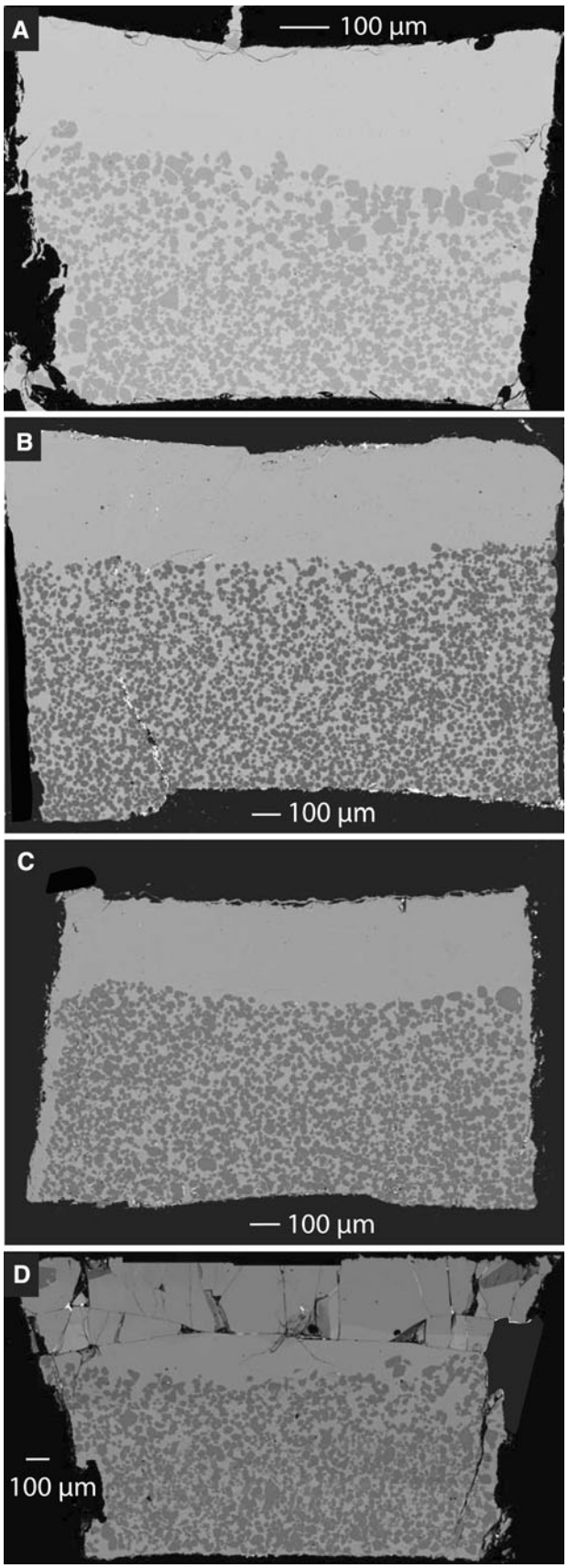

◀**Fig. 2** BSE images of centrifuged samples. **a** ZOB9 (200 g, 1 h) with a grain size of 13 µm and a basal layer porosity of 52 %. The uppermost crystals are not fully settled yet. **b** ZOB6 (200 g, 3 h) with a grain size of 13 µm and a basal layer porosity of 51 %. **c** ZOB4 (400 g, 50 h), the most compacted experiment with a grain size of 18 µm and a basal layer porosity of 30 %. **d** FF05 (700 g, 10 h) with a grain size of 46 µm and a basal layer porosity of 37 %. Olivine is in dark grey, basaltic melt in light grey, and graphite capsule in *black*

±1–2.5 % (1 σ). The porosity difference $\Delta\varphi$ between the uppermost and second segments amounts to 3–8 vol %, and thus, the slope $d\varphi/dh$ from the top to the second layer is poorly defined. Thus, this feature will not be exploited further in this study. Instead, we focus first on the Stokes settling of the sinking olivine grains and secondly on the chemical compaction of the basal olivine layer in the cumulate pile.

Stokes settling of the olivine suspension

The settling velocity of the dense suspension of olivine crystals can be determined from the travel distance of the uppermost crystals of the olivine suspension. As long as the porosity of the top olivine layer remains constant and equal to the bulk porosity, one can assume that these olivine grains are effectively in suspension and do not pile up along grain contacts. A first experiment (ZOB6) centrifuged at 200 *g* for 3 h let to all crystals being settled in a cumulate layer (Table 2). To obtain a crystal layer which top has olivines still floating in the melt, centrifugation had to be decreased to 200*g*, 1 h. In this experiment (ZOB9, Table 2, Fig. 2a), the crystal-free melt layer above the olivine layer has a thickness of 300 ± 30 µm. Hence, the settling velocity of the dense olivine suspension recalculated for an acceleration of 1 *g* is approximately 1.5 µm/h or 4.17(42) 10^{-10} m/s.

Compaction of the olivine layer

The compaction experiments were performed employing different accelerations, run times, and capsule lengths. To rationalize and compare the experimental observations, effective stress over time quantifies the driving force for compaction. For each experiment, the effective stress P_e integrated over time on the olivine in the lowermost segment of the cumulate is

$$\int_o^t P_e \mathrm{d}t = \Delta\rho^{(\mathrm{olivine-basalt})} \cdot h \cdot a \cdot t \qquad (1)$$

where $\Delta\rho^{(\mathrm{olivine-basalt})}$ is the density contrast between crystal and melt (in kg/m^3), h the thickness of the olivine layer above the centre of the lowermost segment (in m), a the experimental acceleration (in m/s^2), and t the time

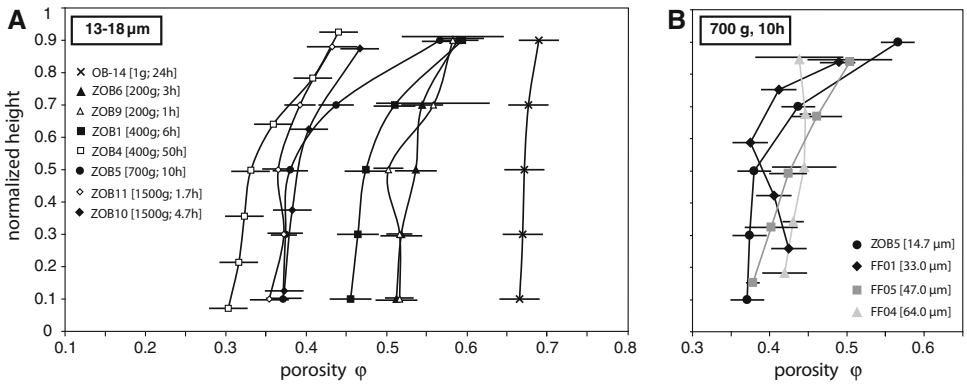

Fig. 3 Porosity profiles with melt abundance or porosity plotted against the normalized total height of the crystal cumulate layers of the experiments. **a** Experiments with grain sizes of 13–18 µm. *Triangles* represent experiments carried out at 200 g; squares those at 400 g; *circles* those at 700 g, and diamonds those at 1,500 g. The run plotted with the crosses is the static experiment of 24 h and represents the starting crystal distribution before centrifuging. **b** Experiments centrifuged at 700*g* for 10 h with different grain sizes

over which the centrifuge acceleration is applied (in s). The density of the olivine is 3,210 kg/m^3, and the density of the liquid is computed to 2,790 kg/m^3 (employing Lange and Carmichael 1990); hence, $\Delta\rho^{(\text{olivine}-\text{basalt})}$ is 420 kg/m^3.

$\Delta\rho^{(\text{olivine}-\text{basalt})}{\cdot}h{\cdot}a{\cdot}t$ is equivalent to pressure multiplied by time. Three observations on the crystal content and the crystal content distribution across the cumulate layer can be made: (1) With increasing $\Delta\rho^{(\text{olivine}-\text{basalt})}{\cdot}h{\cdot}a{\cdot}t$, the average porosity and the porosity in any segment of the cumulate layer decrease (Table 2). In fact, the average crystal content is 34 vol % at static conditions, increases to 45 vol % after 3 h at 200 g (Fig. 2b), and to 63 vol % after 50 h at 400 g (Fig. 2c, Table 2). In the same way, the crystal content in the basal segment increases with centrifugation to 49 vol % (200*g* for 3 h) and further to max. 70 vol % (400 g for 50 h, Fig. 2c). (2) Within each experiment, the crystal content of the crystal layer increases downwards, with dφ/dz being almost constant in the lower 2/3 of the cumulate layer of each experiment (Fig. 3a). (3) With increasing acceleration, an increasing number of crystal contacts are observed in polished sections, and in particular the length over which two crystals touch increases with both effective stress and time (Fig. 4).

The increase in the crystal content with effective stress integrated over time expressed as "applied pressure time" (Fig. 5) can be fit within error with a logarithmic function

$$\varphi_{\text{m}}/\varphi_0 = -0.275(35)\log(\Delta\rho \cdot h \cdot a \cdot t) + 2.82(27) \qquad (2)$$

where φ_{m} is the melt fraction in the bottom layer, φ_0 the melt fraction in the bottom layer after crystal settling (of 0.516 ± 0.017) and which fit quality is $r^2 = 0.88$ (other parameters as in Eq. 1). Similar, the porosity gradient dφ_m/dz, as obtained from fitting all crystal layers except the uppermost one in each sample by a linear equation, correlates best with $\log(\Delta\rho \cdot h \cdot a \cdot t)$ (Fig. 6) confirming the functional form of Eq. (2). The experimental protocol leads to a narrow range of average grain sizes within 11.0–18.6 µm (Table 2) with an average of 14.1 µm. Thus, we have not included grain size as a variable and Eq. (2) is valid for this average grain size.

In order to elucidate the role of grain size, three additional experiments with larger starting grain sizes of 26, 36, and 51.5 µm have been carried out (Table 2) at constant centrifugation time (10 h), gravity acceleration (700 g), and height of the crystal layer (730–740 µm, Table 2). These experiments resulted in mean grain sizes of 33, 47 (Fig. 2d), and 64 µm, however with very broad grain size distributions. Fig. 3b shows the influence of olivine grain size on the porosity profiles in the crystal layer. Scaling the time of adcumulate formation for grain size by multiplying Eq. (2) solved for t with $(d/d_0)^{\text{n}}$, d_0 being 14.1 µm, we calculate the resulting porosity for the grain size scaling exponents $n = 1$, 2, and 3. As can be seen from Fig. 7, the porosities of the basal crystal layer employing larger grain sizes are only slightly less than for 14.1 µm and would be only consistent with a grain size scaling exponent $n = 1$. Such an inverse linear dependency is expected for densification by power law creep (Wilkinson and Ashby 1975) or by reaction-controlled pressure solution creep (Shimizu 1995), the latter being the likely compaction mechanism in this study. Nevertheless, the broad grain size distribution and the untypical porosity profiles for the 33 and 64 µm experiments result in large errors and a large data scatter. We thus consider this result simply as support for a grain size scaling exponent near 1, but further experimentation would be needed to truly constrain this parameter.

Grain growth

With a starting grain size of 1.8 µm, an average grain size d of 13.1 ± 2.5 µm is reached after 24 h of static

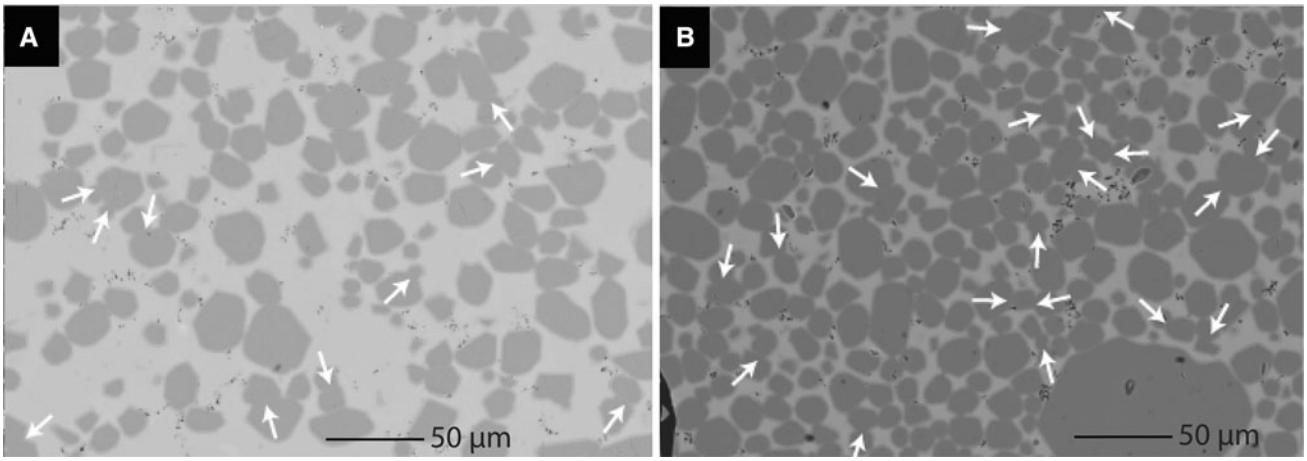

Fig. 4 BSE images illustrating the abundance of crystal contacts. The BSE images are situated between the middle and the bottom of their respective experiments. **a** Picture of experiment ZOB9 with a centrifugation time of 1 h at 200*g*. **b** Picture of experiment ZOB11 with a centrifuging time of 1 h 40 at 1,500*g*. The white arrows show the contacts where chemical compaction is noticeable, demonstrating a clear increase in crystal contacts with effective stress integrated over time

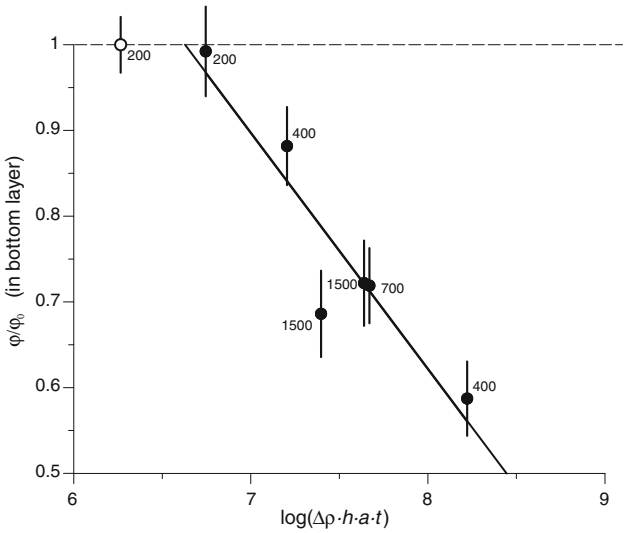

Fig. 5 Porosity of the bottom layer plotted as a function of the logarithm of applied pressure integrated over time. The *solid line* corresponds to the straight line best fitting the experimental data: $\varphi_m/\varphi_0 = -0.275 \log(\Delta\rho \cdot h \cdot a \cdot t) + 2.82$ (Eq. 2), with a correlation coefficient $r^2 = 0.875$. The *dashed line* represents the porosity φ_0 obtained through crystal settling and corresponds to the starting porosity for chemical compaction in the experiments. The *open circle* represents the settling experiment used for determining the aggregate settling velocity where crystals had not fully settled at the end of the experiment

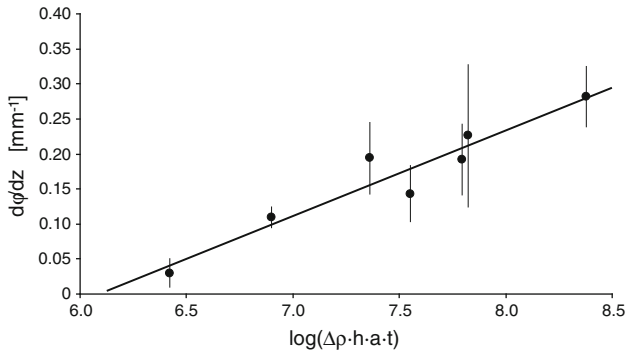

Fig. 6 Vertical porosity gradient for the experiments with grain sizes of 13–18 µm plotted as a function of the logarithm of effective stress integrated over time. In each experiment, all layers, except the uppermost crystal layer (see Fig. 3), were fit by a straight line whose slope is $d\varphi_m/dz$, the porosity gradient. The solid line corresponds to the straight line best fitting the experimental data: $d\varphi_m/dz = 0.122 \log(\Delta\rho \cdot h \cdot a \cdot t) - 0.742$ with a correlation coefficient of $r^2 = 0.915$

equilibration and during centrifugation, further grain growth occurs. The largest final grain sizes for the experiments starting from 1.8 µm amount to 19.1 ± 2.4 µm after 72 h of static growth and to 18.6 ± 2.3 µm for grain growth after 21 h static equilibration and 50 h centrifugation. The olivine crystals show equant shapes with rounded edges. All but two experiments can be fit with a fit quality $r^2 = 0.999$ (Fig. 8) by

$$\log(d) = 0.323(34)\log(t) - 0.47(17) \quad (3)$$

where d is the final grain size (in µm) after run time t (in s). From this fit, we excluded two experiments: Run ZOB10, statically equilibrated for 10 days to attain a grain size of ~80 µm, yielded one anomalously large grain of 500 µm. This large grain remained stuck to the roof of the capsule during centrifugation. All other grains in this experiment form a moderately homogeneous population with an average grain size of 12.3 ± 5.3 µm, which clearly plots below the grain growth curve. Nevertheless, these smaller grains form a compacted olivine cumulus layer. Secondly, run ZOB11 yielded a fairly heterogeneous grain population (11.0 ± 6.6 µm) and would fit Eq. (3) within error, but because of the large error, this value was not used in the dataset fit by Eq. (3).

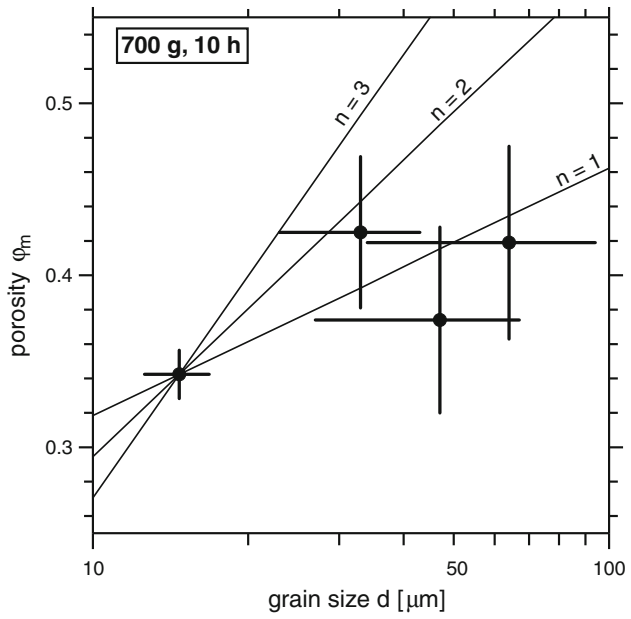

Fig. 7 Porosity φ_m in the basal layer as function of grain size for experiments centrifuged at 700*g* for 10 h. Experiment ZOB5 with an average grain size of 15 μm yielded a porosity of 37 % in the basal layer at a crystal layer height of 450 μm. To render the four experiments comparable, the porosity of ZOB5 was recalculated for a 700 μm crystal layer employing Eq. (2) to 34.2 %. A 700 μm crystal layer is present in the experiments with larger grain size. The lines are the back-calculated porosities for scaling with the grain size exponents $n = 1$, 2, and 3. The experiments with larger grain size would only be coherent with a linear grain size dependence of compaction

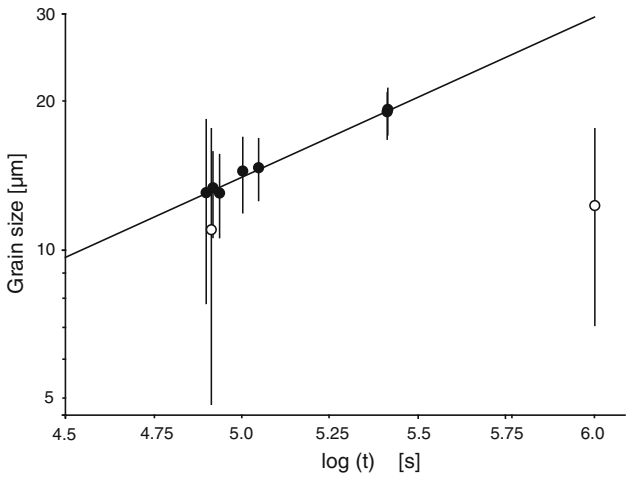

Fig. 8 Mean grain size of olivine plotted as a function of the logarithms of total run time of experiments starting from 1.8 μm grain size. The *solid line* corresponds to the line best fitting the experimental data: $\log(d) = 0.323*\log(t) - 0.47$ with a correlation coefficient of $r^2 = 0.999$. The inverse of the slope of this line corresponds to the grain growth exponent (3.1 ± 0.3), which is similar to value of 3 found by Cabane et al. (2005). The *open symbols* correspond to experiments excluded from the fit (for explanation see text)

The slope of 0.323(34) of Eq. (3) corresponds to 1/n, where n is the growth exponent in the grain growth equation $d^n - d_0^n = k{\cdot}t$, where d is the final grain size after time t, d_0 is the starting grain size and k the ripening rate (for a detailed discussion of Ostwald ripening see Cabane et al. 2005). Thus, our experiments yield a growth exponent of 3.1(3), corresponding closely to the growth exponent $n = 3$ predicted for Ostwald ripening controlled by diffusion in a liquid between large and small grains or by the rate of growth or dissolution at solid–liquid interfaces (Wagner 1961). Similar results have been found by Cabane et al. (2005) for experiments with olivine crystals in silicate melts at 1,250 °C, 1 atm, from which they have established a kinetic law $\sim t^{1/3}$.

Crystal size distributions (CSD) for each experiment are plotted in Fig. 9. The distributions are asymmetric with low abundances towards large grain sizes. For normal grain growth and diffusion-controlled Ostwald ripening, the predicted CSD is narrow, the largest grain size typically smaller than 2× the mean grain size, and the peak in the grain size distribution is located at or slightly above the mean grain size (Lifshitz and Slyozov 1961; Hillert 1965). Our CSD fit these characteristics quite well. Nevertheless, the largest grain sizes in some experiments are higher than 2× mean grain size, but only for a small percentage of grains (~8.4 %).

Normalized crystal size distribution curves for all experiments are plotted in Fig. 10, where grain size is normalized to the mean and the height to the maximum of the grain size distribution. The two experiments that started from 1.8 μm and reached the highest final grain size (OB6 and ZOB4) have exactly the same distribution: narrow with a sharp cut-off of the larger sizes. This kind of distribution is typical for diffusion-controlled Ostwald ripening. In contrast, the experiment with the lowest final grain size (ZOB11) has a distribution with a slight trail to larger sizes, which indicates some contribution from second-order surface reaction controlled growth. Unfortunately, run durations, centrifugation, and final grain sizes could influence this distribution type, in particular as the experiments OB6 and ZOB4 versus ZOB11 are end-members of our run series in terms of run conditions. Nevertheless, the "FF" run series (Table 2), starting from larger grain sizes, also yields narrow CSD matching best with diffusion-controlled Ostwald ripening.

In summary, our CSD, when compared to theoretical models (Hanitzsch and Kalhweit 1969; Lifshitz and Slyozov 1961; Hillert 1965) indicate that the dominant mechanism of grain growth was diffusion-controlled Ostwald ripening. This result is confirmed by our fitted growth exponent of $n = 3.1$ which is similar to $n = 3$ as

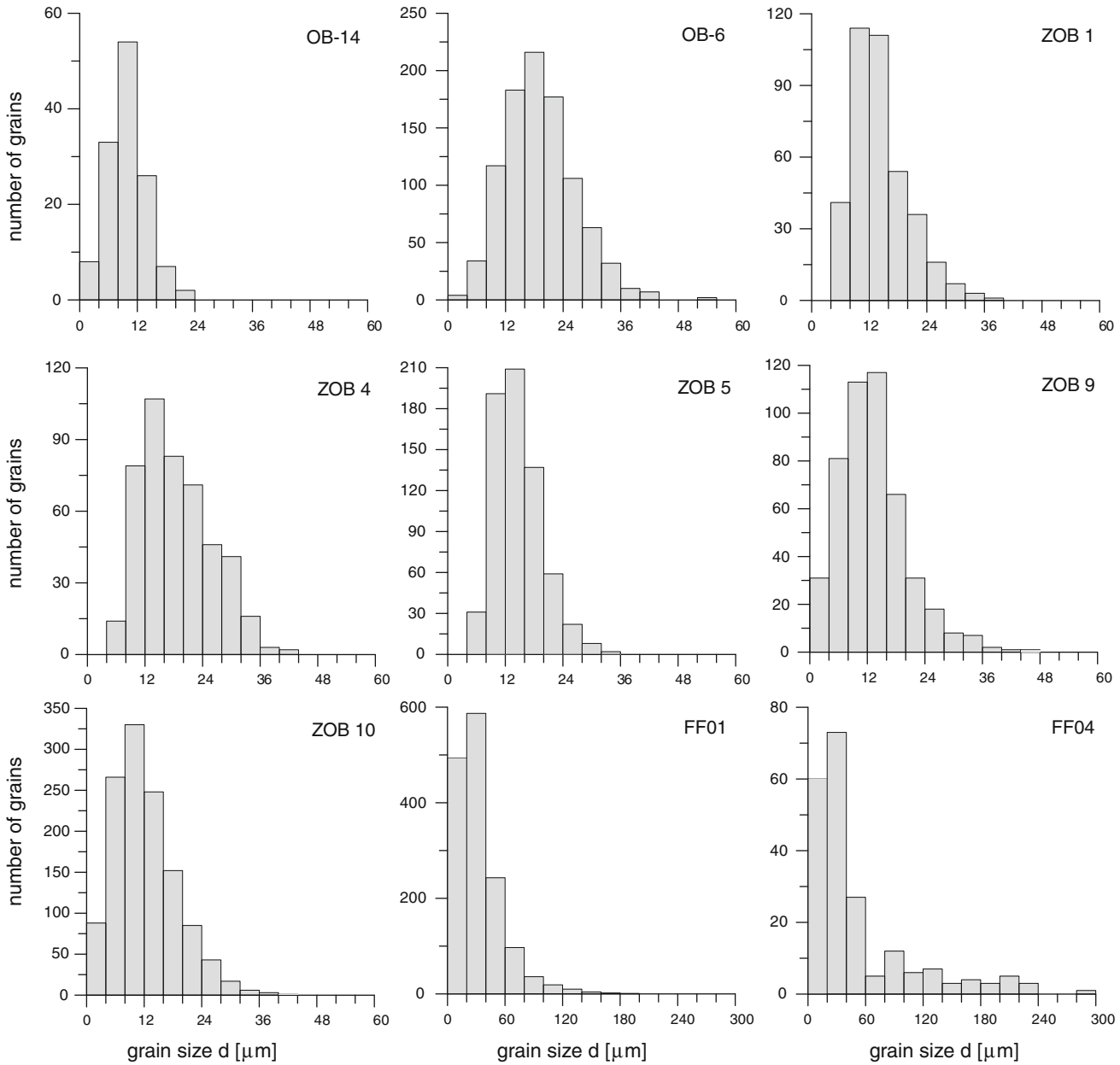

Fig. 9 Histograms of crystal size distributions. The tendency of the distribution is slightly asymmetric with small concentrations towards high values as characteristic for normal grain growth and diffusion-controlled Ostwald ripening

determined by Cabane et al. (2005) for diffusion-controlled Ostwald ripening.

Discussion

Two physical processes dominate during the formation of our experimental cumulates: First, crystals settle through a purely mechanical process in which the olivine grains behave as rigid bodies and form a framework by mechanical compaction (Yang 2000). In nature, this process leads to the formation of orthocumulates (Wager et al. 1960). Nevertheless, for the subsequent compaction process it is of little importance by which mechanism the orthocumulate formed. Once olivines are in contact, compaction occurs through a process which is proportional to effective stress. The most likely mechanism is pressure-induced dissolution and reprecipitation while melt excesses filtrate upwards through the cumulate pile (chemical compaction, Connolly and Podladchikov 2000; see also Schutjens 1991). In nature, this process of adcumulus growth leads to the formation of meso- and adcumulates (Wager et al. 1960).

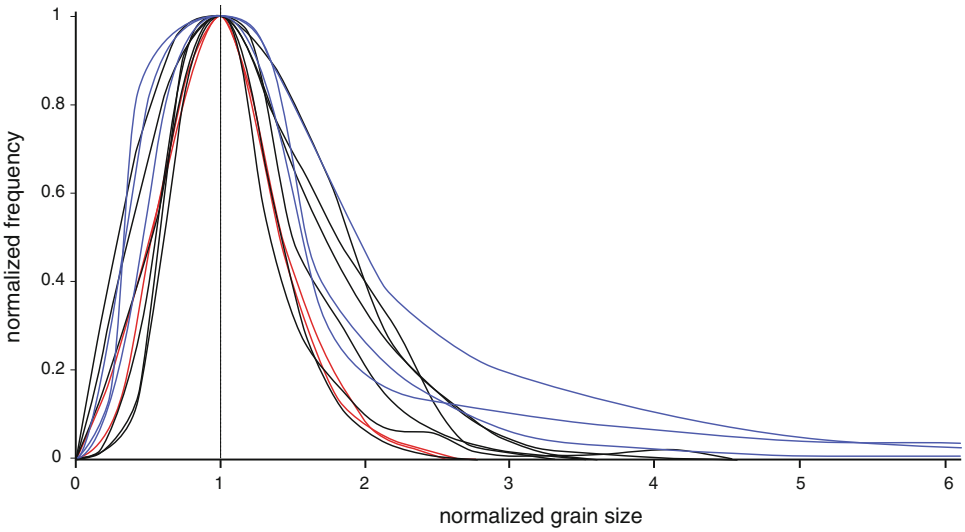

Fig. 10 Normalized crystal size distributions. The grain size is normalized by the mean and frequency of the maximum of the distribution. *Red* static experiments, *black* centrifuged experiments, both on starting grain sizes of 1.8 μm, and *blue* experiments starting from grain sizes larger than 1.8 μm

Stokes settling velocity

To achieve the settling of solid particles dispersed in a liquid, the particles move because gravity acts on the density contrast between the liquid and the solid particle. This purely mechanical process may continue until all grains are in contact to each other, forming a network. In the uncompacted olivine suspension (with 65.9 vol % melt present), grain contacts are not observed (Fig. 1), but this observation is limited because, even in a perfect olivine grain network, only few grain contacts would be observed in a two-dimensional section.

A single grain in an infinite layer of melt settles with a well-defined velocity similar to Stokes' settling velocity (V_s–Stokes 1851), obtained by equating the drag on the settling particle and the buoyancy

$$V_s = \frac{1}{18}\frac{d^2\Delta\rho(n \cdot g)}{\mu} \quad (4)$$

where d is grain size (in m), $\Delta\rho$ the density difference between solid and liquid (420 kg/m^3), $n \cdot g$ the (vertical) acceleration in the system, expressed as a multiple of the gravitational acceleration g, and μ the liquid viscosity (in Pa s). In our experiments, the average olivine grain size, as measured from BSE images of the sample charges OB14, is 13.1 ± 2.5 μm. The viscosity of the melt was calculated to 17 Pa s (Bottinga and Weill 1972). With these parameters, the Stokes settling velocity of olivine grains, scaled to 1 g, is 2.31(74) 10^{-9} m/s. This velocity represents only an approximation because olivine grains are not exactly spherical but short prismatic and thus the drag is slightly different then for a sphere.

When crystals are abundant, a concentrated suspension is formed and the settling velocity becomes either slower or faster than the predicted Stokes velocity. In fact, the distance between grains during the formation of gravitational cumulates is small, that is, typically less than a few grain diameters and the olivines do not settle separately, but all together as a suspension.

In case of a suspension, the velocity of particles is calculated with the "hindered" settling velocity V(ϕ_c), which depends on the concentration of a suspension ϕ_c and follows the semi-empirical relationship (Tomkins et al. 2005):

$$V(\varphi_c) = V_S \cdot (1 - \varphi_c)^n \quad (5)$$

where φ_c is the crystal fraction and n the sedimentation exponent. For fine sand particles, this empirical relationship works up to the dense packing concentration φ_m of 0.74 (tetrahedral or pyramidal packing). With the effectively observed settling velocity $V(\varphi_c) = 4.17(42)\ 10^{-10}$ m/s, and $\varphi_c = 0.341(21)$ (experiment OB14), the sedimentation exponent n in our experiments results to $n \sim 4.1(6)$. High values of n indicate that the average "hindered" sedimentation velocity drops strongly nonlinear down to zero. At high concentrations, settling slows down considerably but does not vanish. Thus, the monodispersed cumulates consisting of crystals deviating from spherical shape experience an extended stage of slow settling at concentrations close to the dense packing ϕ_m.

Schwindinger (1999) investigated the settling of clay prisms in a viscous liquid, because they have a similar shape to olivine grains. She observed that for a solid fraction in the suspension of $\varphi_c \sim 0.35$ (i.e. 35 vol %), which is very close to that of our samples after static equilibration (34.1 vol %), the suspension settles as a single object with a speed of 0.1 V_S. Applied to our suspensions, this would lead to a settling velocity of 2.3 × 10^{-10} m/s or 0.8 μm/h at 1 g. We observe that the settling velocity in experiment ZOB9 reaches 4.2 × 10^{-10} m/s, that is, 1/6 Stokes velocity. This number supports

Schwindinger's (1999) conclusions and excludes aggregate settling velocities for natural cumulates much lower than 1/6 Stokes velocity.

Porosity of the gravitationally settled olivine cumulate

The porosity after Stokes settling of the olivine crystals is 54 ± 3 vol % (ZOB6, ZOB9). The experiments do not define a more precise value for two reasons: In the experiments with the lowest acceleration and run time, the cumulate surface is rough (Fig. 2a) such that porosity cannot be determined exactly at the surface. However, centrifugal forces cause an immediate onset of chemical compaction in the cumulate layer. As soon as a self-supporting network of grains forms, a small porosity gradient develops even in the least compacted experiment.

The experimental result agrees well with the commonly purported estimate of ~60 vol % porosity of orthocumulates (Irvine 1980; Shirley 1986, for discussion see Tegner et al. 2009), a value that stems from both theoretical considerations and measurements. We thus recommend a final porosity of 54 vol % for orthocumulates build of equant grains (e.g. olivine, cpx; but not plagioclase). From the experimental and from the measured porosities of orthocumulates, it follows further that the porosity of natural crystal piles formed through mechanical settling remains far from that of a dense cubic packing of spheres of 37 %.

Pressure-induced dissolution and reprecipitation–chemical compaction

After grain settling, further densification of the cumulate layer may be reached through grain rotation and chemical compaction. The effect of grain rotation during initial compaction, just after grains make contact to each other, is thought to be of less importance. In the present study, it cannot be separated from the effect of chemical compaction and may contribute a few per cent to the decrease in porosity.

Evidence for "welding", that is more frequent olivine grain contacts, is already found in the centrifuge experiments with the lowest "pressure · time" values (ZOB6). The porosity of 30.3 vol % of the most compacted experiment (ZOB4) is significantly below that of the initial porosity of orthocumulates of 54 vol % and also below the most dense cubic packing of spheres with 37 % porosity. For most experiments, there is ample evidence for large grain contact areas (Fig. 4), that is, in a two-dimensional section many and long contacts between individual grains can be observed.

The observations that the amplitude of compaction is proportional to effective stress integrated over time together with the increase in grain contact area indicates that pressure dissolution of olivine is the dominant mechanism of compaction. This mechanism leads to larger crystal contact areas per unit volume and to a reduction in porosity through a change in shape of the olivine grains. Pressure dissolution in contact areas and reprecipitation of the same material where grains are in contact with the interstitial liquid requires short diffusion distances in the melt. The change in grain shape occurs at the expense of (but not from) the interstitial liquid. During pressure-driven compaction, grain growth continues and, in principal, also a contribution of surface energy-driven Ostwald ripening is possible. Nevertheless, compaction in the experiments is proportional to effective stress integrated over time but not to time alone, and thus, the time-dependent Ostwald ripening process appears of second-order importance for recrystallization during compaction.

A detailed analysis of the fine structure of olivine grain boundaries yields further evidence for a dissolution–reprecipitation process of olivine. The first feature is the presence of Ca, which is characteristic only for MORB melt, at the interface of two adjacent olivine grains even when no melt is present. Analyses have been carried out at the boundary between two adjacent olivine grains as well as towards the interior (Fig. 11a). Table 3 presents analyses on welded olivine grain boundaries after centrifugation, which should be compared to the analysis of Table 1. Olivine at the welded grain boundaries has lower SiO_2 and FeO concentrations and higher MgO contents than in the grain interior. The presence of Ca in the grain boundary region (Fig. 11b) can be attributed to grain dissolution or recrystallization. The Ca concentration is high in the melt phase and at the starting point of the grain junction, but is also at an increased level within the boundary layer between the two olivine grains were no melt is present.

Images obtained by high-resolution electron microscopy (HREM) have allowed identifying the fine structure of the boundary between two adjacent olivine grains (Fig. 11d,e) which are compared to an olivine–melt contact (Fig. 11f). The upper left part of Fig. 11f is an olivine crystal (i.e. the crystalline phase) and on the lower right side the melt phase (i.e. the amorphous phase). The thickness of the recrystallized boundary layer is not more than 2 nm. In Fig. 11d and e, the recrystallized boundary layer between two olivine grains is 4–6 nm. The boundaries between two olivine grains are distinct but not as fully crystallized as the interior of olivine grains. This indicates that some chemical species from the MORB melt (e.g. Ca) prevent the recrystallization of olivine in a perfectly crystalline structure.

These observations can best be explained by a dissolution and reprecipitation of olivine. This process is driven by the centrifuge-induced pressure on grain contacts. Non-hydrostatic pressure is proportional to the height of the olivine column above the measured section, the density

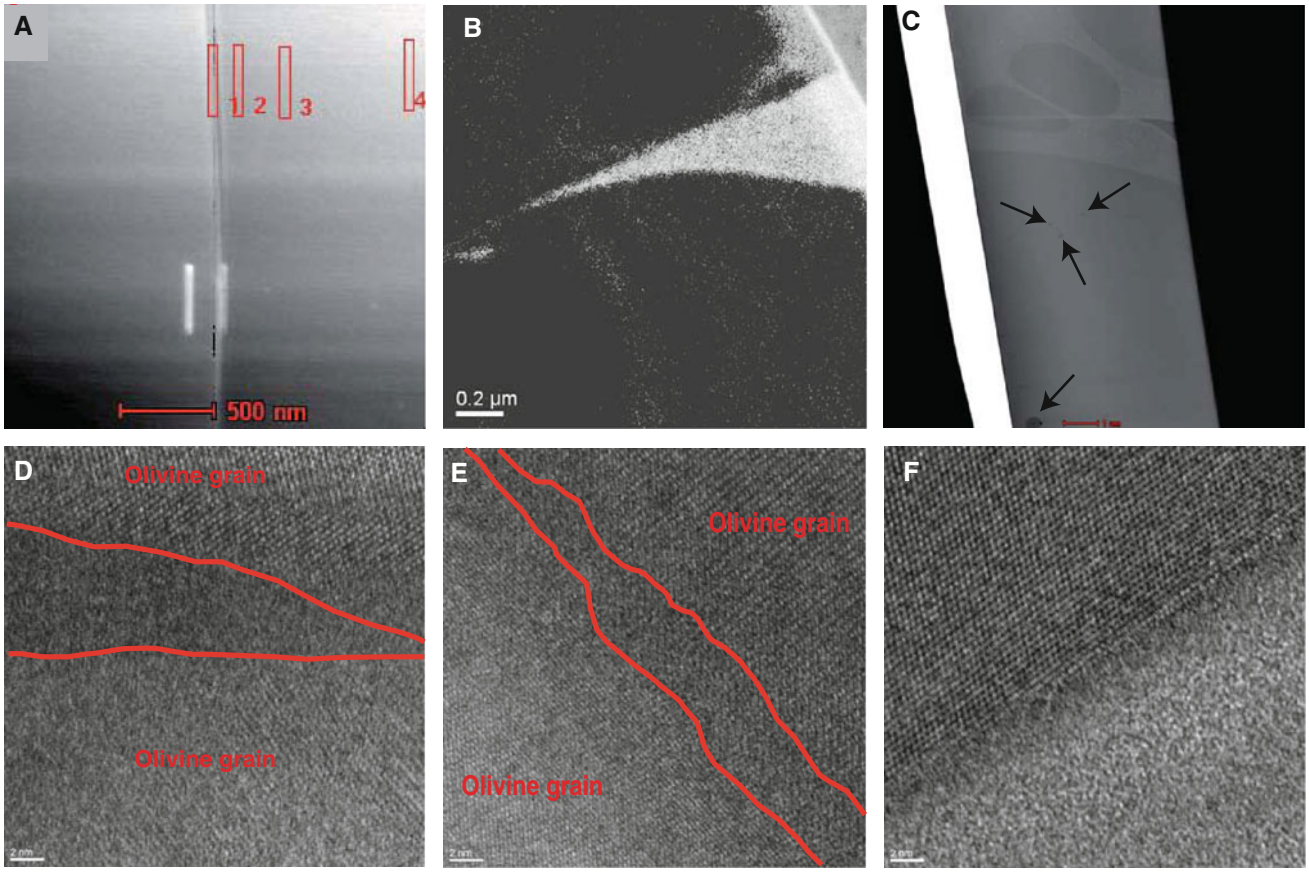

Fig. 11 Fine structure of olivine grain boundaries. **a** Contact of two adjacent Ol-grains with analyses positions in ZOB10 sample (see Table 3). **b** Calcium map near triple junction between two grains and a melt pocket. Brightness is proportional to Ca concentration. **c** Overview of one grain boundary in sample ZOB10. The *black arrows* indicate inclusions. **d** and **e** HREM Images showing boundary between two olivines in the sample ZOB10 and ZOB11, respectively. **f** HREM Image showing a boundary between melt (amorphous phase) and one olivine grain (crystallized phase) in sample ZOB10

Table 3 Chemical composition for the different positions situated between two olivine grains (for the point 1) and then towards the centre of one olivine grain (for the points 2, 3, and 4) (see Fig. 11) in experiment ZOB10

Oxides	1 (wt%)	2 (wt%)	3 (wt%)	4 (wt%)
SiO_2	35.70	35.40	33.80	37.30
TiO_2	0.06	0.00	0.00	0.00
FeO	4.60	3.40	4.00	3.70
Al_2O_3	0.30	0.00	0.20	0.00
MgO	58.90	61.00	61.80	58.70
CaO	0.40	0.20	0.20	0.20
Total	99.96	100.00	100.00	99.90

contrast between olivine and liquid, and the centrifugal acceleration. The non-hydrostatic stress leads to dissolution and a basaltic liquid oversaturated in olivine, which in turn causes reprecipitation on the grain surfaces in contact with the liquid. This process increases the grain contact area to distribute the effective stress over a larger surface (Connolly and Podladchikov 2000). A complete review of the literature about pressure solution mechanisms and its modelling goes beyond the purposes of this study and can be found in Angevine and Turcotte (1983), Tada and Siever (1989), Shimizu (1995) and Fowler and Yang (1999). The non-hydrostatic or lithostatic pressure (P_p) for our olivine grains in the basal segment can be quantified through

$$P_p = (1 - \varphi_m) \cdot \Delta\rho^{(\text{olivine}-\text{basalt})} \cdot h \cdot a \quad (6)$$

where φ_m is porosity, $\Delta\rho$ the density difference between solid and liquid (420 kg/m^3), h the height of the cumulate layer (in m), and a gravity acceleration. P_p amounts to 0.6–2.5 kPa in the experiments that resulted in porosities <40 % in the basal layer. This value is similar to the pressure of 1.4 kPa at the base of a cumulate of ½ m height and a porosity of 35 %, that is, values typical for compacted olivine cumulates in nature.

The observation of a much stronger porosity gradient in the uppermost third of the crystal layer than in the lower two-thirds is most likely a combined result of boundary

effects and the effect of melt escaping from the compacting cumulate (Jaupart and Tait 1995). The total height of the experimental cumulate layers varies between 420 and 740 μm, sectioned into 4–7 layers, each of them around 100 μm in thickness. Each layer has thus an average thickness of 8–9 grains, and the uppermost layer is strongly influenced by, for example, the roughness of the cumulate layer surface. Nevertheless, such a strong gradient at the top boundary was observed in theoretical models of viscous compaction with an upper impermeable boundary (Yang 2001).

The low porosity limit of chemical compaction

Chemical compaction will slow down when the decreasing permeability of the adcumulate leads to a hindered escape flow of the excess melt. Whether this applies to our experiments can be evaluated by comparing the hydrostatic pressure gradient ∇P_h (Eq. 7) with the lithostatic pressure gradient ∇P (Eq. 8).

$$\nabla P_h = q \cdot \mu / k \tag{7}$$

$$\nabla P = (1 - \varphi_m) \cdot \Delta\rho \cdot a \tag{8}$$

where q is the melt flux expressed as $h \cdot \Delta\varphi/t$, μ is melt viscosity (17 Pa·s) and k permeability calculated from $k = \frac{d^2}{c} \cdot \varphi_m^3/(1 - \varphi_m)^2$, where $c = 10$ (Connolly et al. 2009), φ_m is porosity, $\Delta\rho$ the density contrast between melt and solid of 420 kg/m^3, and a the experimental acceleration. Hydrostatic pressure gradients for the experiments result to $\nabla P_h = 0.4 - 220 \times 10^3$ Pa/m, and lithostatic pressure gradients ∇P are 0.3–4 $\times$ 10^6 Pa/m. The hydrostatic over lithostatic pressure gradient in the experiments then results to 10^{-2}–10^{-3} and thus $\ll 1$, and we conclude that our experiments are not permeability limited.

At the same time, the above Eqs. (7) and (8) can be used to approximate the lower bound of porosity to which pressure dissolution–reprecipitation would operate as compaction mechanism. At this porosity threshold, melt escape becomes hindered by the concomitant decrease in permeability. In the experiments, with melt fluxes $h \cdot \Delta\varphi/t$ of 0.4–5.7 $\times$ 10^{-9} m/s, the hydrostatic pressure gradient ∇P_h would equal the lithostatic pressure gradient ∇P at residual melt fractions φ_m of 0.03–0.05. At these porosities, the upward-directed melt escape would counterbalance the downward-directed force exerted by the crystal pile and hence compaction would slow down and effectively cease.

The above-calculated lower porosity threshold for compaction may be compared to trapped liquid estimates in natural layered intrusions. In natural cumulates that formed a closed system upon final trapping of an interstitial melt, the amount of trapped liquid can be recalculated from trace element concentrations of incompatible elements which are not contained in the cumulate phases. The trapped liquid concept has been criticized by Meurer and Boudreau (1998) and Meurer and Meurer (2006) on the basis of an analysis of mafic cumulates from the Stillwater complex, where different incompatible traces yield vastly different trapped liquid estimates. Meurer and Meurer (2006) argue that in Stillwater, the interstitial liquid remained part of an open system to almost zero porosity. However, Tegner et al. (2009) argue that in Skaergaard compaction (and intercumulus melt expulsion) pre-dates crystallization of the interstitial remnant melt, such that incompatible trace element concentrations can be used to estimate the amount of trapped liquid. Coherent results are obtained from P, U, and Rb bulk concentrations, demonstrating that the Middle and Upper Zones of the Skaergard intrusion typically crystallized 4.8 ± 2.1 wt% (1 σ) interstitial melt, with 90 % of the samples containing between 2 and 7 wt% crystallized residual melt. This estimate is in good agreement with the calculated lower limit of porosity attainable through chemical compaction.

Formation times of gravitational cumulates

Typical natural cumulate layers of olivine amount to ≤½ m in thickness, with typical average grain sizes of 2–10 mm (Goode 1976; Wiebe 1988). On the other hand, the total height of cumulate piles under compaction (constituted by a multitude of layers) in large layered mafic intrusions is only limited through cooling from the gravitational bottom. Tegner et al. (2009) argue that in Skaergaard compaction occurred predominantly in the top few tens of metres of the crystal mush. As typical end-members we thus discuss first the formation and compaction times of a single ½-m-thick olivine layer, secondly compaction times at the basis of a 50-m-thick cumulate pile, and third, derive the compaction height enabling compaction to the lower porosity threshold of chemical compaction.

Crystal settling and orthocumulates

Orthocumulates may form through mechanical Stokes settling from a (magmatic) suspension or through other mechanisms such as gravity slumps and density currents. For Stokes settling, settling distances result from the thickness of the orthocumulate layer and the initial crystal fraction in the unsettled suspension. The settling time can then be calculated as

$$t_{ortho} = (h \times 0.46/\varphi_{ci} - h)/V(\varphi_c) \tag{9}$$

where h is the thickness (in m) of the uncompacted orthocumulate layer, and $V(\varphi_c)$ the hindered Stokes settling velocity (in m/s) calculated from Eq. (5). The factor 0.46

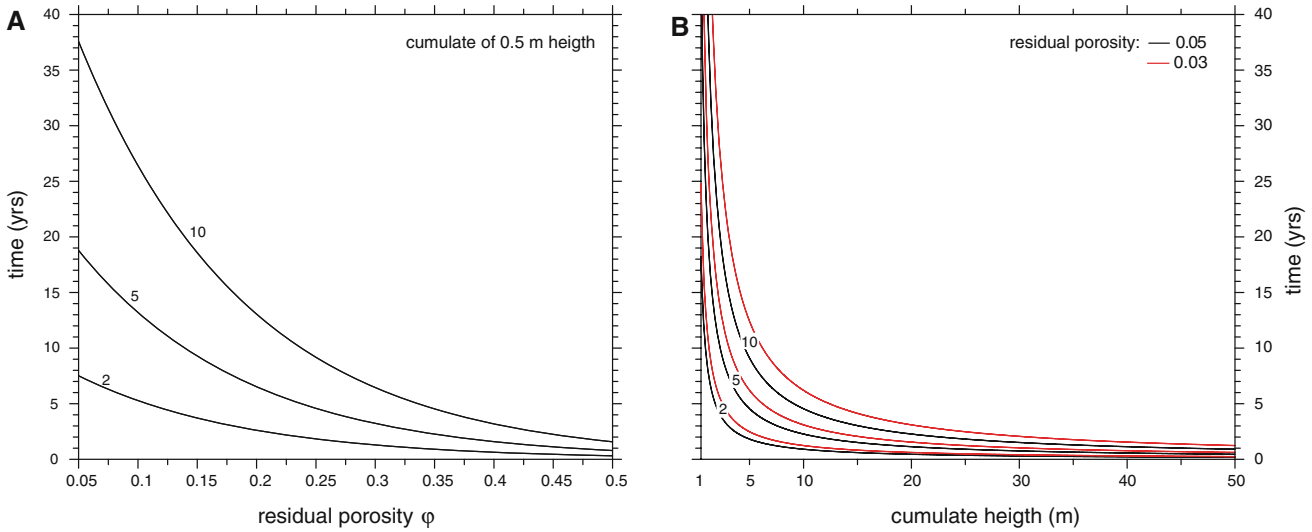

Fig. 12 Cumulate compaction times calculated from Eq. (10). **a** Compaction or adcumulate formation times for a single standing ½-m-thick cumulate layer of olivine for different grain sizes (2, 5, and 10 mm) for variable final porosities. **b** Compaction time as a function of compaction height (i.e. the height of the simultaneously compacting crystal pile) for residual porosities of 0.05 and 0.03, that is, the porosity range of the compaction limit. Complete compaction of cumulate piles >20 m thick can be expected within a few years. Numbers on the *curves* indicate grain sizes in mm. Residual porosities are those at the basis of the cumulate layer or pile

corresponds to the crystal fraction after gravitational settling while φ_{ci} denotes the initial crystal fraction in the melt layer from which the orthocumulate forms. The time necessary to produce 1 m of an uncompacted crystal layer of olivine is thus 242, 39, or 10 h for an initial crystal content $\varphi_{ci} = 0.01$ for grain sizes of 2, 5, or 10 mm, respectively. For an initial crystal fraction $\varphi_{ci} = 0.05$, these values become 52, 8.4, and 2.1 h. It can thus be concluded that the hindering of the crystal settling due to the formation of a dense suspension does not slow down orthocumulate formation decisively. As will be seen in the next section, chemical compaction is an order of magnitude slower.

Compaction and adcumulus growth

Regardless whether an initially little or uncompacted crystal mush was formed by crystal settling or another mechanism, the gravitationally driven compaction of this crystal pile can be modelled from our experimental results. Equation (2), derived from the experiments, yields the time dependence of chemical compaction for constant grain size (14 μm) and can thus be employed to calculate meso- and adcumulate formation times. To scale for grain size, we introduce a linear grain size dependence as appropriate for a dissolution-precipitation limited process (Boudreau and McBirney 1997; Shimizu 1995, see also Neijmeijer et al. 2009) and as consistent with the experiments. The compaction time t_{adcum} (in s), that is the time necessary to reduce porosity from $\varphi_0 = 0.54$ to φ_m in the basal layer of a cumulate of height h_{cum} (in m), can be calculated as

$$t_{adcum} = \left(\frac{1.803 \times 10^{10}}{10^{\frac{\varphi_m}{0.1487}}} - 4.2123 \times 10^6\right) \times \frac{1}{h_{cum} \cdot g \cdot \Delta\rho^{crystal-melt}} \cdot \frac{d}{d_0} = \left(\frac{1.308 \times 10^{14}}{10^{\frac{\varphi_m}{0.1487}}} - 3.0561 \times 10^{10}\right) \frac{d}{h_{cum} \cdot \Delta\rho^{crystal-melt}} \quad (10)$$

where d is grain size (in m), d/d_0 is the grain size scaling factor with $d_0 = 14.1 \times 10^{-6}$ m (from the experiments), $\Delta\rho$ is the density contrast between crystals and melt (in kg/m^3), and g is the Earth's gravity. Note that Eq. (10) has h_{cum} in the denominator, as pressure dissolution–driven chemical compaction in the basal layer is the faster the thicker the crystal pile and thus effective stress is.

Formation times of meso- or adcumulates from orthocumulate layers with a starting porosity of 54 % are then calculated for olivine (Fig. 12). For a single standing ½-metre olivine cumulate, chemical compaction will result in a residual porosity of 30 vol % at grain sizes of 2, 5, and 10 mm after 0.37–1.9 years. To reach 20 or 10 % residual porosity, 1.8–8.9 and 8.4–42 years, respectively, are necessary for grain sizes of 2–10 mm (Fig. 12a).

When considering a compacting cumulate pile of 50 m height (possibly constituted by multiple layers), formation times decrease proportionally: 30 % porosity at the base of such a cumulate pile is achieved after 1–7 days, 20 % after 7–32 days, and 10 % porosity after 31–153 days for 2–10 mm grain sizes (Fig. 12b).

These periods of orthocumulate and adcumulate formations may first be compared to characteristic cooling times of magma sills, which are in the order of years to decades, depending on the sill thickness and the level of intrusion. The solidification of a dike or sill of half width b can be calculated as a function of thermal conductivity K, density ρ_r, heat capacity c, temperature T_0 of the country rock, of the intrusion temperature T_m and the latent heat L of the intruding magma (Turcotte and Schubert 2002, equations in "Appendix"). In the case of mafic layered intrusions, it is appropriate to select basaltic material also as country rock and K, L, ρ_r, and c are then the material properties of broadly basaltic material, typically $K = 2.5$ W m^{-1} K^{-1}, $L = 420$ kJ kg^{-1}, $\rho_r = 2{,}750$ kg m^{-3}, and $c = 1$ kJ kg^{-1} K^{-1}. With these values, the thermal diffusivity κ results to 9.1×10^{-7} m^2 s^{-1}. T_m can be assumed to be at or slightly less than the liquidus temperature of basaltic material at a few kbar and is around 1,250 °C. The two parameters which then remain to be constrained are the half thickness b of the sill and background temperature T_0. If we remain with a ½-m adcumulate with 30 % porosity, the sill half thickness is constrained by the initial crystal content φ_{ci} to 18–4 m for 1–5 % olivine crystals in the melt layer or sill magma. Typically, large layered mafic intrusions intrude at a few kbar depth equivalent, leading to a background temperature of 300–550 °C. Furthermore, the characteristic cumulates are not formed at the very beginning of the history of a large layered mafic intrusion; hence, it is plausible that a first series of sills or magma chambers has further heated the surroundings, possibly leading to background temperatures of 500–700 °C or more. At 4–18 m half sill thickness, $T_0 = 400$ °C leads to characteristic cooling times of 0.5–9.0 years, $T_0 = 550$ °C to 0.6–12 years and $T_0 = 700$ °C to 0.8–15 years. Comparing the formation times of a single ½-m olivine adcumulate with these characteristic cooling times gravitationally driven olivine adcumulate formation of single layers appears generally feasible to residual porosities of 30–20 %. To achieve lower residual porosities in a single cumulate layer, thicker cumulate piles and hence thicker sills (or magma chambers) would be required.

Layered mafic intrusions are constituted by a multitude of layers that may compact simultaneously, that is, within a given cumulate layer compaction continues during deposition (and compaction) of successive layers. In this case, crystal piles of hundreds of metres are feasible (e.g. at Skaergard or Bushveld) and compaction would proceed to the compaction limit as long as the interstitial liquid has not cooled down (from the bottom) such that precipitation of non-cumulus phases starts. As detailed above, the lower limit of porosity to be achieved by chemical compaction is 3–5 vol %. With a crystal pile of 50 m, the compaction limit of $\varphi_m = 0.05$ is already achieved after 66–330 days (for 2–10 mm grain size, Fig. 12b), and >20 m of crystal cumulates are sufficient to approach the compaction limit within a few years.

In principal, the porosity profile across individual cumulate layers becomes more homogeneous with an increasing height of the compaction zone, and from the porosity gradient within a layer, one could derive the height of the cumulate pile leading to compaction of the cumulate layer.

Conclusions

From our experiments, four conclusions are drawn: (1) the settling velocity for a dense suspension with an olivine fraction of 0.34 is fast (1/6 of the Stokes velocity); for example, for an olivine grain size of 5 mm, the suspension velocity will be approximately of 22 cm/h. (2) Mechanical settling of olivine yields crystal fractions of 0.46 at most. (3) The prevailing process of compaction is pressure dissolution of olivine at grain boundary contacts followed by precipitation of olivine on the pore walls. This chemical compaction ultimately resulting from a lithostatic pressure in the crystal pile that is larger than the hydraulic pressure in the magma yields feasible time scales of compaction as long as this mechanism scales linearly with grain size. (4) Typical formation times for a single ½-m-thick olivine layer with 25–30 % porosity at its basis is 4 months to 3 years, while (5) compaction readily completes to its lower porosity threshold of 3–5 % at the base of >20-m-thick piles of cumulates as characteristic for large layered mafic intrusions. The compaction of both a single cumulate layer and a cumulate pile occurs on time scales that are realistic when compared to characteristic cooling times of magma sills or chambers of appropriate thickness.

We conclude that purely gravitationally driven compaction of cumulates to 80–95 % olivine content (or probably any other crystal species with similar shape and similar or greater density contrast to the melt) is geologically fast and feasible.

Acknowledgments This work was supported by ETH grant TH 20/03-2 and by SNF grant 200020-111725-1. NB thanks ETH for a visiting professor fellowship. We thank Neil Baker, now at Broadbent Lim., for engineering the centrifuge and B. Zürcher for constant improvements and maintenance of the centrifuging piston cylinder set-up.

Appendix

The solidification of a dike or sill is given by Turcotte and Schubert (2002):

$$t_s = \frac{b^2}{4\kappa\lambda^2} \tag{11}$$

where at $t = t_s$, all magma has solidified and where b is the half width of the sill, κ the thermal diffusivity of the country rock and λ the roof of

$$\lambda(1 + erf\ \lambda)e^{\lambda^2} = \frac{c(T_m - T_0)}{L\pi^{1/2}} \quad (12)$$

where c is the specific heat capacity of the country rock, T_m the intrusion temperature of the magma, T_0 the temperature of the country rock, and L the latent heat of solidification. The thermal diffusivity κ is defined by:

$$\kappa = \frac{K}{\rho_r c} \quad (13)$$

where K is the thermal conductivity and ρ_r the density of the country rock.

References

Akatsuka T, Obata M, Yokose H (1999) Formation of layered structure in the Murotomisaki gabbroic complex, especially picrite gabbro, Kochi prefecture, Japan–qualitative evaluation of crystal accumulation. J Geol Soc Jap 105:771–788 (in Japanese with English abstract)

Angevine CL, Turcotte DL (1983) Porosity reduction by pressure solution: a theoretical model for quartz arenites. Geol Soc Am Bull 94:1129–1134

Bohlen SR, Essene EJ, Boettcher AJ (1980) Reinvestigations and applications of olivine-quartz-orthopyroxene barometry. Earth Planet Sci Lett 47:1–10

Bose K, Ganguly J (1995) Quartz-coesite revisited: reversed experimental determinations at 500–1,000 °C and retrieved thermochemical properties. Am Mineral 80:231–238

Bottinga Y, Weill DF (1972) The viscosity of magmatic silicate liquids: a model for calculation. Am J Sci 272:438–475

Botto L, Narayanan C, Fulgosi M, Lakehal D (2005) Effect of near-wall turbulence enhancement on the mechanisms of particle deposition. Int J Multiphase Flow 31:940–956

Boudreau AE, McBirney AR (1997) The Skaergaard layered series. Part III. Non-dynamic layering. J Petrol 38:1003–1020

Cabane H, Laporte D, Provost A (2005) An experimental study of Ostwald ripening of olivine and plagioclase in silicate melts: implications for the growth and size of crystals in magmas. Contrib Mineral Petrol 150:37–53

Chen CF, Turner JS (1980) Crystallization in a double-diffusive convective system. J Geophys Res 85:2573–2593

Chipman J (1926) The Soret effect. J Am Chem Soc 48:2577–2589

Connolly JAD, Podladchikov YY (2000) Temperature-dependent viscoelastic compaction and compartmentalization in sedimentary basins. Tectonophys 324:137–168

Connolly JAD, Schmidt MW, Solferino G, Bagdassarov N (2009) Permeability of asthenospheric mantle and melt extraction rates at mid-ocean ridges. Nature 462:209–212

Conrad ME, Naslund HR (1989) Modally-graded rhythmic layering in the Skaergaard intrusion. J Petrol 30:251–269

Cygan RT, Carrigan CR (1992) Time-dependent Soret transport-applications to brine and magma. Chem Geol 95:201–212

Dorfman A, Dingwell DB, Bagdassarov NS (1997) A rotating autoclave for centrifuge studies: falling sphere viscometry. Eur J Mineral 9:345–350

Fowler AC, Yang X (1999) Pressure solution and viscous compaction in sedimentary basins. J Geophys Res B 104:12989–12997

Gasquet D, Fernandez A, Mahé C, Boullier AM (1995) Origine des rubanements dans les granitoïdes : exemple du monzogranite de Brignogan-Plouescat (NW du Massif armoricain). Comptes Rendus de l'Académie des Sciences Series 2(321):369–376

Goode ADT (1976) Small scale primary cumulus igneous layering in the Kalka layered intrusion, Giles Complex, central Australia. J Petrol 17:379–397

Hanitzsch E, Kalhweit M (1969) Zur Umlösung aufgedampfter Metallkristalle, II. Zeitschrift Phys Chem 65:290–305

Hillert M (1965) On the theory of normal and abnormal grain growth. Acta Metall 13:227–238

Holness MB, Cheadle MJ, McKenzie D (2005) On the use of changes in dihedral angle to decode late-stage textural evolution in cumulates. J Petrol 46:1565–1583

Hort M, Marsh BD, Spohn T (1993) An oscillatory nucleation model for igneous layering. Contrib Mineral Petrol 114:425–440

Hoshide T, Obata M, Akatsuka T (2006) Crystal settling and crystal growth of olivine in magmatic differentiation–the Murotomisaki Gabbroic Complex, Shikoku, Japan. J Mineral Petrol Sci 101: 223–239

Huppert HE, Sparks RSJ (1984) Double-diffusion convection due to crystallization in magmas. Ann Rev Earth Planet Sci 12:11

Irvine TN (1980) Magmatic infiltration metasomatism, double-diffusive fractional crystallization, and adcumulus growth in the Muskox intrusion and other layered intrusions. In: Hargraves RB (ed) Physics of magmatic processes. Princeton University Press, Princeton, pp 325–383

Irvine TN (1987) Layering and related structures in the Duke Island and Skaegaard intrusions: Similarities, differences, and origins. In: Parsons I (ed) Origins of igneous layering. Series C: Math Phys Sci 196: 666 p

Irvine TN, Keith DW, Todd SG (1983) The J-M platinum-palladium Reef of the Stillwater Complex, Montana: II. Origin by double-diffusive convective magma mixing and implications for the Bushveld Complex. Economic Geol 78:1287–1334

Irvine TN, Andersen JCO, Brooks CK (1998) Included blocks (and blocks within blocks) in the Skeargaard intrusion:geological relations and the origins of rhythmic modally graded layers. Geol Soc Am Bull 110:1398–1447

Jaupart C, Tait S (1995) Dynamics of differentiation in magma chamber. J Geophys Res 100:17615–17636

Kadik AA, Lebedev EB, Dorfman AM (1989) Modeling of separation process of magmatic melts from crystals using high-temperature centrifuge. Geokhimiya 1:43–54

Kerr RC, Turner JS (1982) Layered convection and crystal layers in multicomponent systems. Nature 298:731–733

Lange RL, Carmichael ISE (1990) Thermodynamic properties of silicate liquids with emphasis on density, thermal expansion and compressibility. Rev Mineral 24:25–64

Langmuir CH (1989) Geochemical consequences of in situ crystallization. Nature 340:199–205

Lesher CE, Walker D (1988) Cumulate maturation and melt migration in a temperature gradient. J Geophys Res 93:10295–10311

Lifshitz IM, Slyozov VV (1961) The kinetics of precipitation from supersaturated solid solutions. J Phys Chem Solids 19: 35–50

Lucas SB, St-Onge MR (1995) Syn-tectonic magmatism and the development of compositional layering, Ungava Orogen (northern Québec, Canada). J Struct Geol 17:475–491

McBirney AR, Nicolas A (1997) The Skaergaard Layered Series. Part II. Magmatic flow and dynamic layering. J Petrol 38:569–580

McBirney AR, Noyes RM (1979) Crystallization and layering of the Skaergaard Intrusion. J Petrol 20:487–564

Meurer WP, Boudreau AE (1998) Compaction of igneous cumulates part I: geochemical consequences for cumulates and liquid fractionation trends. J Geol 106:281–292

Meurer WP, Meurer MES (2006) Using apatite to dispel the "trapped liquid" concept and to understand the loss of interstitial liquid by compaction in mafic cumulates: an example from the Stillwater complex Montana. Contrib Mineral Petrol 151:187–201

Naslund HR, McBirney AR (1996) Mechanisms of formation of igneous layering. In: Cawthorn RG (ed) Layered intrusions. Elsevier, Amsterdam, pp 1–43

Neijmeijer A, Elsworth D, Marone C (2009) Significant effect of grain size distribution on compaction rates in granular aggregates. Earth Planet Sci Lett 284:386–391

Parsons I (ed) (1987) Origins of igneous layering. NATO ASI Series, Reidel Publishing Co, Dordrecht, pp 287–312

Raedecke LD, McCallum IS (1984) Investigations in the Stillwater complex: 2. Petrology and petrogenesis of the ultramafic series. J Petrol 25:395–420

Robins B, Haukvik L, Jansen S (1987) The organization and internal structure of cyclic units in the Honningsvåg intrusive suite, North Norway: implications for intrusive mechanisms, double-diffusive convection and pore-magma infiltration. In: Parsons I (ed) Origins of igneous layering. NATO ASI Series, Reidel Publishing Co, Dordrecht, pp 287–312

Roeder PL, Dixon JM (1977) A centrifuge furnace for separating phases at high temperature in experimental petrology. Can J Earth Sci 14:1077–1084

Schmidt MW, Connolly JAD, Günter D, Bogaerts M (2006) Element partitioning: the role of melt structure and composition. Science 312:1646–1650

Schutjens PMTM (1991) Experimental compaction of quartz sand at low effective stress and temperature conditions. J Geol Soc 148: 527–539

Schwindinger KR (1999) Particle dynamics and aggregation of crystals in a magma chamber with application to Kilauea Iki olivines. J Volc Geotherm Res 88:209–238

Shimizu L (1995) Kinetics of pressure solution creep in quartz. Tectonophys 245:121–134

Shirley DN (1986) Compaction of igneous cumulates. J Geol 94: 795–809

Stokes GG (1851) On the effects of the internal friction on the motion pendulums. Trans Camb Phil Soc 9:8–106

Tada R, Siever R (1989) Pressure solution during diagenesis. Ann Rev Earth Planet Sci 17:89–118

Tatum JA, Finnis MV, Lawson NJ, Harrison GM (2005) 3-D particle image velocimetry of the flow field around a sphere sedimenting near a wall Part 2. Effects of distance from the wall. J Non-Newtonian Fluid Mech 127:95–106

Tegner C, Thy P, Holness MB, Jakobsen JK, Lesher CE (2009) Differentiation and compaction in the Skaergaard intrusion. J Petrol 50:813–840

Tomkins MR, Baldock TE, Nielsen P (2005) Hindered settling of sand grains. Sedimentology 52:1425–1432

Tory EM, Pickard DK (1977) A three-parameter Markov model for sedimentation. Can J Chem Eng 55:655–665

Tory EM, Pickard DK (1986) Experimental evidence for a stochastic approach to sedimentation. In: Moudgil BM, Somasundaran P (eds) Flocculation, sedimentation and consolidation. AIChE, NY, The Cloister, Sea Island, GA Jan 27–Feb 1, 1985, 297–306

Turcotte DL, Schubert G (2002) Geodynamics: application of continuum physics to geological problems. Wiley, New York 450 pp

Wager LR (1959) Differing powers of crystal nucleation as a factor producing diversity in layered igneous intrusions. Geol Mag 96: 75–80

Wager LR, Brown GM (1968) Layered igneous rock. Edited by Oliver and Boyd, Edinburgh and London, p 588

Wager LR, Brown GM, Wadsworth WJ (1960) Types of igneous cumulates. J Petrol 1:73–85

Wagner C (1961) Theorie der Alterung von Niederschlägen durch Umlösen. Zeitschrift Elektrochem 65:581–591

Wiebe RA (1988) Structural and magmatic evolution of a magma chamber: the Newark Island layered intrusion, Nain, Labrador. J Petrol 29:383–411

Wilkinson DS, Ashby MF (1975) Pressure sintering by power law creep. Acta Metal 23:1277–1285

Wilson JR, Larsen SB (1985) Two-dimensional study of a layered intrusion: the Hyllingen Series, Norway. Geol Mag 122:97–124

Wilson JR, Menuge JF, Pedersen S, Engell-Sorensen O (1987) The southern part of the Fongen-Hyllingen layered mafic complex, Norway: emplacement and crystallization of compositionally stratified magma. In: Parsons I (ed) Origins of igneous layering. Reidel Publishing Co, Dordrecht, NATO ASI Series, pp 145–184

Yang X (2000) Pressure solution in sedimentary basins: effect of temperature gradient. Earth Planet Sci Lett 176:233–243

Yang X (2001) Density driven compactional flow in porous media. J Comp Appl Math 130:245–257